Iron ligands and isotopes in hydrothermal plumes over backarc volcanoes in the Northeast Lau Basin, Southwest Pacific Ocean

Hu Wang [a, *], Meitong Liu [a], Wenpeng Wang[a], Huaiyang Zhou [a], Michael J. Ellwood [d], David A. Butterfield [b,c], Nathaniel J. Buck [b,c], Joseph A. Resing [b, c]

[a] State Key Laboratory of Marine Geology, Tongji University, Shanghai 200092, PR China

[b] Cooperative Institute for Climate, Ocean, and Ecosystem Studies, University of Washington, Seattle, WA 98115, USA

[c] Pacific Marine Environmental Laboratory-NOAA, Seattle, WA 98115, USA

[d] Research School of Earth Sciences, Australian National University, Canberra, Australia

Abstract

Deep-sea hydrothermal venting is an important source of dissolved iron (dFe) to the oceans. Fe isotopes can be used as a potential tool to trace the dispersal of hydrothermal plumes. However, Fe isotope fractionation and its relation with Fe speciation as hydrothermal plumes disperse is still poorly constrained. In this study, we determined the Fe speciation and total and dissolved Fe isotope composition (δ^{56}tFe, δ^{56}dFe) for several hydrothermal plumes from backarc volcanoes in the Northeast Lau Basin. This combined approach provides important insights into the evolution of Fe isotopes in hydrothermal plumes. The results suggest δ^{56}tFe variation in plumes is related to the loss of particulate Fe-sulfides or Fe-oxyhydroxides (FeOOH), both of which are dependant on the H_2S concentrations and Fe/H_2S in the source hydrothermal fluids. δ^{56}dFe compositions in the hydrothermal plumes increase during plume dispersal/dilution and can be as high as 0.85‰, demonstrating that hydrothermal plumes can export dissolved Fe with a significantly heavier δ^{56}dFe than hydrothermal fluids. The reasons may be ascribed to the organic Fe complexes (FeL) and colloidal FeOOH in the dissolved phase. Another interpretation might be associated with the low pH in volcanic arc hydrothermal systems rich in magmatic

CO_2 and SO_2, which decreases the Fe(II) oxidation rate. Further, we demonstrate for the first time that the δ^{56}dFe is positively correlated with the conditional stability constants of FeL ($\log K'_{FeL}$). A Rayleigh distillation model is presented based on the mass balance of the determined FeL, and colloidal FeOOH in hydrothermal plumes, which can explain the observed Fe isotope compositions in hydrothermal plumes. Our data show how Fe isotopes are transformed within a hydrothermal plume above arc volcanoes and how these may differ from that of the original vent fluids. It adds to our understanding of the processes that have an impact on the Fe speciation and isotope composition in deep-sea hydrothermal plumes.

Keywords: iron isotopes, organic iron complexation, hydrothermal plumes, arc volcano, Northwest Lau Basin

1. INTRODUCTION

Iron is an essential nutrient for the growth of oceanic phytoplankton and exerts great influence on the primary productivity and carbon cycling in the oceans, making it necessary to investigate the supply and removal of Fe and to understand its geochemical cycle in the oceans (Martin et al., 1990; Archer and Johnson et al., 2000; Boyd and Ellwood, 2010; Boyd et al., 2017; Tagliabue et al., 2017). Recently, it has been shown that hydrothermally sourced Fe can be transported thousands of kilometers away from where it was initially vented making it an important Fe source contributing to the oceanic Fe budget (Fitzsimmons et al., 2014, 2017; Resing et al., 2015; German et al., 2016; Moffett and German, 2020). The long-range transport is ascribed to the formation of organic Fe complexes and colloidal Fe in hydrothermal plumes (Lang et al., 2006; Bennett et al., 2008, 2011; Toner et al., 2009; Sander and Koschinsky et al., 2011; Yücel et al, 2011; Hawkes et al., 2013a; Gartman et al, 2014; Findlay et al., 2015; Wang et al., 2019, 2021a).

Iron stable isotopes can be used as a potential tracer of hydrothermally sourced Fe (Nishioka et al., 2013; Conway and John et al., 2014; Fitzsimmons et al., 2014;

Resing et al., 2015). The light dissolved Fe isotope (δ^{56}dFe) signal above the TAG (Trans-Atlantic Geotraverse) vent site within the Mid-Atlantic Ridge rift valley at 500 m suggest that hydrothermal venting not only affects the δ^{56}Fe of the deep ocean but also impacts seawater at depths < 1000 m (Conway and John, 2014). However, there are very few studies on the characteristics of Fe isotope systematics in hydrothermal plumes, and Fe isotope fractionation during plume rise and dispersal remains unconstrained.

Previously, it has been demonstrated that pyrite (FeS_2) particles formed in the buoyant part of hydrothermal plumes are isotopically light δ^{56}Fe relative to vent fluids, which shifts the remaining dissolved Fe (dFe) towards a heavier δ^{56}dFe (Bennett et al., 2009; Lough et al., 2017; Klar et al., 2017; Nasemann et al., 2018; Wang et al., 2021b). In contrast, Fe-oxyhydroxides formed after Fe-sulfide production are isotopically heavy, thereby resulting in a lighter δ^{56}dFe (Severmann et al., 2004; Bennett et al., 2009; Rouxel et al., 2016; Klar et al., 2017; Lough et al., 2017; Nasemann et al., 2018). However, due to difference in vent chemistry (Fe, H_2S concentrations and δ^{56}Fe of the fluids, etc.), both the dissolved and particulate δ^{56}Fe vary significantly during plume rise and dispersal and show large regional variability (Severmann et al., 2004; Bennett et al., 2008; Lough et al., 2017). Studies of Bennett et al. (2008) and Rouxel et al. (2016) revealed that particles from the buoyant plumes over basalt-hosted hydrothermal vents (5°S Mid-Atlantic Ridge and 9°50´N East Pacific Rise) were isotopically lighter than the source vent fluids. This was attributed to the influence of Fe-sulfide precipitation. However, Severmann et al. (2004) sampled the buoyant plume particles from the Rainbow vent on the Mid-Atlantic Ridge and found that the particles there had heavier δ^{56}Fe (0.15~1.20‰) than the source vent fluids (-0.14‰). They reasoned that this was due to vent fluids percolating through ultramafic host rocks resulting in fluids with very high Fe/H_2S (~24) (Douville et al., 2002). Here, the low amounts of sulfide relative to Fe indicates that Fe-oxyhydroxide precipitation is the dominant dissolved iron removal process,

with no more than 4% of Fe forming sulfides (Severmann et al., 2004). More recently, the measured δ^{56}dFe and its fractionation have been shown to vary with plume dynamics. For example, δ^{56}dFe in a buoyant plume above the East Scotia Ridge located in the Southern Ocean decreased during plume dispersal due to Fe(II) oxidation and the formation of particulate Fe-oxyhydroxides (Lough et al. 2017). In contrast, Wang et al. (2021b) demonstrated that the δ^{56}dFe in diluted buoyant plumes from the Beebe vent field located in the Mid-Cayman ultraslow-spreading ridge system increased from -4.08‰ to 0.22‰, due to Fe(II) oxidation, the exchange of Fe between the particulate and dissolved Fe and between inorganic Fe and organic Fe complexes. In non-buoyant plumes, it was found that δ^{56}dFe increased with plume dilution (Fitzsimmons et al., 2017; Klar et al., 2017). Further, Nasemann et al. (2018) investigated Fe isotope fractionation in plumes above the Nifonea vent field, New Hebrides Back-Arc in Southwest Pacific Ocean and measured heavier δ^{56}Fe values than vent fluids. They ascribe these heavy values to the sulfide-rich basalt-hosted hydrothermal systems coupled with slow oxidation kinetics, which helped stabilize the dissolved Fe.

Although it is known that the complexation of Fe by organic ligands may affect the δ^{56}dFe of hydrothermal plumes (Klar et al., 2017; Nasemann et al., 2018), it has not been systematically investigated before. Previous experimental studies in laboratory settings suggests that the complexation of Fe by desferrioxamine B (DFOB), which can be produced by bacteria and fungi in the oceans to acquire Fe, favours heavier isotopes in the Fe-DFOB complex relative to that of inorganic Fe(III) (Dideriksen et al., 2006; Morgan et al., 2010). By contrast, theoretical calculations using molecular orbital/density functional theory predicted an equilibrium fractionation of -0.34‰ between Fe(III)-DFOB and Fe(III) (Domagal-Goldman et al., 2009). Therefore, more experimental data are needed to clarify the influence of organic complexation on Fe isotope fractionation.

Taken together, the dissolved and particulate isotope signals released from deep-sea

hydrothermal systems into the overlying deep-ocean can be constrained using a mass balance approach which accounts for Fe-sulfide formation, Fe-oxyhydroxide precipitation and Fe complexation with organic ligands. So far, most studies using Fe isotopes as a process tracer have been conducted in hydrothermal fields situated at mid-ocean ridges and backarc basins. No studies have used Fe isotopes to characterize hydrothermal plumes above arc volcanoes. The chemical observations made along volcanic arcs (Massoth et al., 2003; de Ronde et al., 2007; Resing et al., 2007, 2009; Neuholz et al., 2020; Kleint et al., 2022) have shown that the chemical enrichment of CO_2, SO_2 and H_2S in the hydrothermal plumes above arc volcanoes appear to be much greater than those in plumes above mid-ocean ridges.

The aim of this study is to investigate the isotope composition of dFe and total Fe (tFe) in combination with Fe complexation analysis of organic Fe-binding ligands in the hydrothermal plumes above rear arc volcanoes in the Northeast Lau Basin to resolve the fractionation mechanisms of Fe isotopes. We present the relationship between the Fe isotope and Fe-binding ligands. This will add to our understanding of the regional variations and provide new insights into how Fe isotopes are transformed within a hydrothermal plume and how these may differ from that of the original vent fluid. Understanding the processes in hydrothermal plume that lead to changes in $\delta^{56}Fe$ can greatly improve the Fe biogeochemical models in global oceans.

2. Geological setting

The Northeast Lau Basin is located in the western Pacific Ocean in Tongan territorial waters, North of the main Tongan Islands and southwest of the Samoan Islands (Figure 1). It is part of the Tonga subduction system, at which the Pacific Plate is being subducted westward beneath the Indo-Australian Plate. The Northeast Lau Basin hosts the Earth's highest subduction rates and fastest-opening backarc basin with widespread hydrothermal activity and submarine volcanic eruptions (Bevis et al., 1995; Zellmer et al., 2001). The submarine Mata volcano assemblage is located

between the Tonga Trench and the NE Lau Basin spreading center, and contains nine elongate en echelon volcanoes oriented in a WSW-ENE direction (Fig. 1) (Rubin and Embley, 2012). The northern seven volcanoes from Mata Fitu to Mata Taha are oriented in a WSW direction and have summit depths ranging from 1900 to 2400 m. The southern West and East Mata volcanoes are oriented in a ENE direction and have summit depths of 1200 and 1330 m (Baker et al., 2019; Resing et al., 2011).

West Mata is one of only two places in the world where deep-sea submarine eruptions have been witnessed (Resing et al., 2011), and it is probably the best-studied rear arc volcano. Many magmatic hydrothermal systems dominate the West Mata volcano. As a result, the hydrothermal fluids emanating from the West Mata have high concentrations of SO_2, CO_2, S and H_2 (Resing et al., 2011; Baumberger et al., 2014), which are very different from water/rock dominated systems which tend to have high H_2S concentrations (de Ronde and Stucker, 2015).

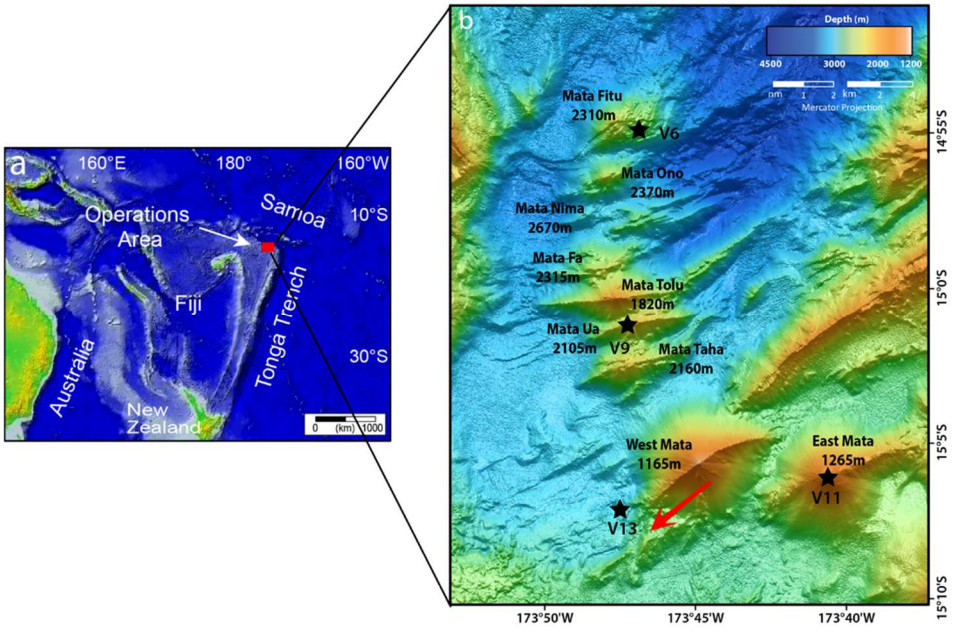

Fig.1. Location of the study area (a). Bathymetric map of Mata volcanoes and the locations of four vertical casts (b) (Fig.1a based on Resing et al., 2011). The red arror indicates the direction of plume dispersion at West Mata.

3. MATERIALS AND METHODS

3.1. Hydrothermal plume detection and sampling

Hydrothermal plume samples (30 totally) were collected for Fe ligand and isotope analysis from 4 vertical hydrocasts during the Northeast Lau Basin cruise (FK171110) on the R/V Falkor from November 10-21, 2017. The vertical casts of V6, V9 and V11 were conducted over Mata Fitu, Mata Ua and East Mata volcanoes, respecitvely. V13 cast was conducted about 5 km away from the summit of West Mata volcano to track the change of Fe isotopes during plume dispersal. These plumes were detected and sampled using a CTD profiler system combined with optical backscatter and oxidation-reduction potential (ORP) sensors, which were mounted on a stainless steel frame with 21 trace metal clean 17.5 L Niskin-style sampling bottles with epoxy-coated springs. Plumes were identified and sampled based on positive turbidity and negative ORP anomalies (Fig. 2a-d). Most samples collected were situated in non-buoyant plumes, although three samples (V9-2, V9-8 and V11-2) show slightly lighter density values than the water immediately above and below them (see supplementary data), which we ascribed to the mixing and drag from the CTD package itself or the turbulence at the edges of the buoyant portion of the plume. In addition, V13 cast had two distinct plume layers. The deep plume might be related to the syn-eruptive transport of volcanic ash, which can sink down deeper than the venting site (Walker et al., 2019).

Upon recovery, samples for total Mn (tMn, as a proxy for plume dilution) and tFe concentration and δ^{56}tFe analysis were collected directly from the sampling bottles into low-density polyethylene bottles (LDPE, Nalgene) and acidified to pH < 2 with sub-boiling distilled HCl. All the LDPE bottles were pre-cleaned using first detergent solution followed by rinsing with distilled water, and then soaking in 3M HCl (analytical grade) for 4 days at 60°C while turning the bottles several times, and finally by thorough intermediate rinsing with Milli-Q water. Those clean bottles were filled with 0.01 M sub-boiling distilled HCl until shipping. Samples for dissolved Mn (dMn) and dFe concentrations and δ^{56}dFe analysis were obtained by pressurizing

Niskin bottles with N_2 gas and passing samples through Supor membrane (0.2 μm) filters (Pall Inc.) into LDPE bottles and acidified to pH < 2. A subset of filtered samples was stored immediately at -20°C for Fe-binding ligand analysis. In order to examine nano particulate Fe in dissolved phase, about 10 mL of the filtered samples were passed through 0.025 μm polycarbonate filters for colloidal analysis.

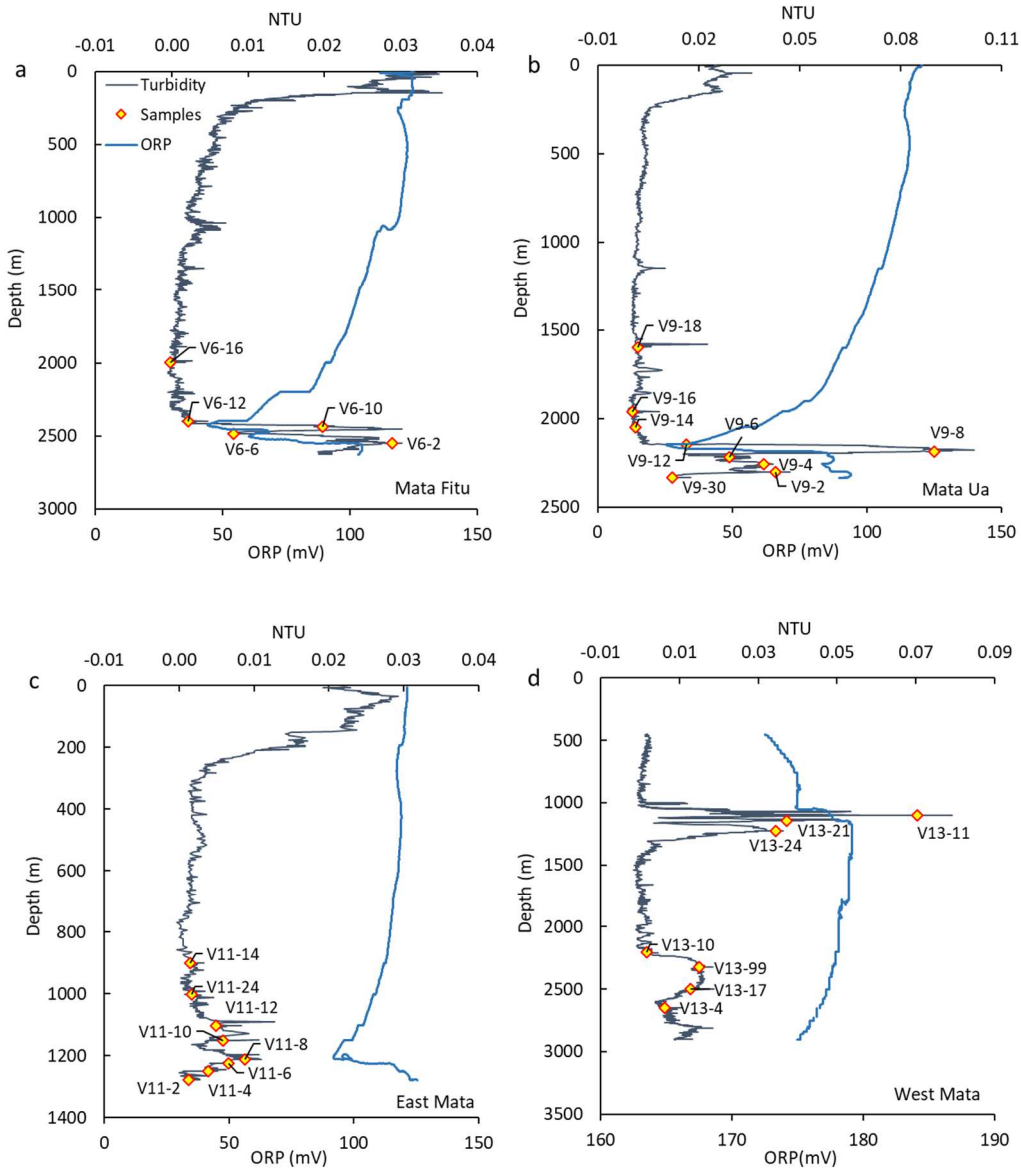

Fig. 2. (a)-(d) Turbidity signal and ORP data at the locations of Mata Fitu (V6), Mata Ua (V9), East Mata (V11) and the flank of West Mata (V13) samples.

3.2. Fe isotope and concentrations analysis

Total and dissolved Fe isotopes and concentrations were determined using the procedures outlined by Ellwood et al. (2020). Briefly, water samples were spiked with

200 a ^{57}Fe-^{58}Fe double spike and left overnight to equilibrate, after which they were
201 buffered to a pH of 4.5 with a trace-metal clean ammonium acetate buffer and then
202 passed over 0.5 mL columns packed with Nobias PA Chelate PA1L resin
203 (Hitachi-Hitec, Japan). After matrix removal using ammonium acetate buffer, samples
204 were eluted with 1 mol L^{-1} HNO_3 and were evaporated to dryness and redissolved in
205 0.5 mL 6 mol L^{-1} HCl. Then, they were further purified using an anion exchange resin
206 (AG-MP1, BioRad Laboratories, U.S.A.). After sample loading, 3 mL of 6 mol L^{-1}
207 HCl was passed through the column to remove any seawater matrix and ions that may
208 interfere with the Fe isotope analysis. Iron was eluted from the anion exchange resin
209 with 3 × 1 mL of 0.5 mol L^{-1} HCl. Samples were evaporated to dryness and
210 redissolved in 1 mL of 2% (w w^{-1}) HNO_3.
211 Iron isotopes were determined on a Thermo Neptune Plus MC-ICP-MS (Thermo
212 Scientific, Germany) at the Australian National University (ANU) in Canberra,
213 Australia, equipped with an APEX-IR sample introduction system (Elemental
214 Scientific, U.S.A.) and X-type skimmer cones (Ellwood et al., 2015).
215 Analysis by MC-ICP-MS was conducted in high-resolution mode in order to
216 resolve polyatomic interferences. ^{54}Cr and ^{58}Ni were also monitored and used to
217 correct ^{54}Fe and ^{58}Fe from elemental overlap. Instrumental mass bias was corrected
218 for using the ^{57}Fe-^{58}Fe double spike approach. Iron isotope compositions are reported
219 in delta notation relative to the Fe isotope standard IRMM-014 (^{56}Fe/^{54}Fe=15.6985)
220 and expressed in per mill [‰] as described in Eq. (1) below.

221 $$\delta^{56}\mathrm{Fe} = \left[\frac{(\quad/^{4}\quad)_{\mathrm{Sample}}}{(\quad/^{4}\quad)_{\mathrm{Standard}}} - 1\right] \times 10^{3} \qquad (1)$$

222 As a check of method reproducibility, an in-house standard was run multiple times
223 with the samples and produced a value of 0.43 ± 0.09 ‰ (n = 9, mean ± 2 standard
224 deviation).
225 tFe and dFe concentrations for each sample were calculated using sample weight
226 and the amount of double spike added to the sample. This calculation is based on
227 isotope dilution using the known proportion of ^{58}Fe in the ^{57}Fe-^{58}Fe double spike.

3.3. Determination of tMn and dMn

The tMn and dMn, as a conservative tracer of plume dilution, were determined by direct-injection flow injection analysis (Resing and Mottl, 1992) as modified by Resing et al. (2009) at National Oceanic and Atmospheric Administration - Pacific Marine Environmental Laboratory (NOAA-PMEL). In brief, Mn concentrations were determined by spectrophotometric detection of the malachite green formed from the reaction of leucomalachite green and potassium periodate with Mn acting as a catalyst. The replicate analyses (n = 10) of standards indicated the precision of tMn and dMn is ± 1 nM or 3% (whichever is greater). The accuracy of Mn measurement was assured by running an internal standard at least once daily.

3.4 Determination of Fe-binding ligands

The organic Fe(III)-binding ligands concentration ([L]) and their conditional stability constants of (K'_{FeL}) were determined using the reverse-titration competitive ligand exchange-adsorptive cathodic stripping voltammetry (RT-CLE-ACSV) method, considering that the dFe concentrations were higher than ligand concentrations in hydrothermal plumes (Hawkes et al., 2013b; Wang et al., 2019). Due to the limited volume, only the ligands of Mata Ua and West Mata plume samples were analyzed. The full details of RT-CLE-ACSV theory using the competitive ligand 1-nitroso-2-naphthol (1N2N) are detailed elsewhere (Hawkes et al., 2013b; Wang et al., 2019). In brief, subsamples (10 ml) were pipetted into 12 polytetrafluoroethylene (PTFE) vials. Borate buffer solution (75 μL) was added to each vial to yield a final pH = 7.8 (on the seawater scale) similar with that of plume samples. Variable amounts of stock NN solution were added to 12 vials, to yield final concentrations ranging from 0.5 to 40 μM 1N2N in the vials. These solutions were allowed to equilibrate overnight (typically > 12 hours) at room temperature (~ 25℃). The samples were then transferred to a Teflon cell cup and purged with high purity nitrogen for 3 minutes, followed by the determination of $Fe(NN)_3$ by ACSV. The deposition potential was -0.05 V for 1-5 minutes (depending on the Fe concentrations) while the solution was

stirred with a rotating PTFE rod (1200 rpm); after a quiescence period of 10 s, the potential was scanned from -0.15 V to -0.7 by sampled-DC at 50 mV/s. The [L] in a sample and K'_{FeL} were determined by fitting of the RT-CLE-ACSV equation introduced in Hawkes et al. (2013b) and Wang et al. (2019). One ligand model was used considering it can provide a better fit to the measured data than two ligand model.

3.5. Scanning electron microscopy and energy-dispersive X-ray spectroscopy for colloidal analysis

About 1cm^2 of 0.025 μm polycarbonate filters was glued on metal stub coated with 10 nm of pure carbon to assure electric conductivity. The images and associated chemical compositions of colloids were examined with a field emission-scanning electron microscopy (FE-SEM, TESCAN Mira 3, Czech) equipped with an energy-dispersive X-ray spectroscopy (Oxford Ultim Max40 EDS). The SEM and EDX were operated at 10-15 kV and 15 kV of accelerating voltage, respectively.

4. RESULTS

4.1. tFe and dFe concentrations in the hydrothermal plume

The tFe concentrations in V6 (Mata Fitu), V9 (Mata Ua), V11 (East Mata) and V13 (West Mata) plume samples were similar, varying from 4.7 nM to 156.1 nM, 5.0 nM to 97.0 nM, 7.2 nM to 33.6 nM, and 12.1 nM to 67.0 nM respectively, and the dFe concentrations ranged from 1.6 nM to 86.1 nM, 2.8 nM to 72.8 nM, 3.8 nM to 26.2 nM, and 5.1 nM to 27.8 nM (Table 1). dFe had a linear relationship with tFe and constituted a significant portion of tFe, 49.5 ± 11.1%, 66.1 ± 8.3%, 61.5 ± 19.1% and 49.2 ± 29.6% for Mata Fitu, Mata Ua, East Mata and West Mata samples, respectively. Organic Fe complexes and colloidal Fe may be the likely explanation for the high dFe proportion to the tFe pool. Previous studies conducted over West Mata showed significant higher concentrations of tFe and tMn, which can be 3275 and 359 nM, respectively. Those high Fe and Mn concentrations were from plume samles over the

West Mata summit. However, our samples were about 5 km away from West Mata summit.

4.2 tFe and dFe isotope composition in the hydrothermal plume

The tFe isotope compositions (δ^{56}tFe) in Mata Fitu and Mata Ua plumes were similar, ranging from -0.6 to -0.17‰ and -0.7 to 0.27‰ (Table 1). For East Mata and West Mata samples, tFe isotope compositions ranged from -0.68 to 0.15‰ and -0.09 to 0.64‰. The dFe isotopes (δ^{56}dFe) show a wider range with values ranging from -1.69 to 0.85‰, -1.13 to 0.55‰, -0.45 to 0.68‰ and -1.01 to 0.64‰ for Mata Fitu, Mata Ua, East Mata and West Mata plume samples, respectively. The reason may be attrubuted to the dFe isotope fraction caused by various processes in plume such as Fe oxidation, precipitation and complexation with organic ligands.

4.3. tMn and dMn concentrations in the hydrothermal plumes

Concentrations of tMn were 158.5 nM, 89.9 nM, 27.5 nM, 30.5 nM in near vent plume samples, and down to 8.0 nM, 4.4 nM, 7.2 nM, 6.2 nM in more dispersed samples (Table 1). The strong relationship between tMn and dMn (dMn making up near 100% of tMn) indicates that Mn behaves near-conservatively during hydrothermal plume mixing allowing us to use Mn as a tracer of plume dilution during this study (Massoth et al., 1994; James and Elderfield, 1996; Field and Sherrell, 2000).

4.4. Fe ligands in hydrothermal plumes

The $\log K'_{FeL}$ found in Mata Ua and West Mata samples were between 19.6 ± 0.41 and 21.4 ± 0.15 (mean ± standard deviation of two replicate measurement, Table 1). Ligand concentrations varied from 1.73 ± 0.04 to 11.06 ± 0.66 nM and were consistently lower than dFe concentrations, which is consistent with previous studies on Fe-binding ligands in hydrothermal plumes (Bennett et al., 2008; Hawkes et al., 2013a; Buck et al., 2015; Wang et al., 2019).

4.5. SEM and EDX analyses

Several different colloid types were identified, with the first being poorly

crystallized minerals composed solely of Fe and O, which we interpret to be colloidal (0.025 ~ 0.2 μm diameter) Fe-oxyhydroxides. The morphology and element composition of colloidal particles from Mata Fitu and West Mata were shown in Fig. 3a and 3b (similar colloids from Mata Ua and East Mata not shown). In addition, we also observed colloids mainly composed of Fe, Si, Al, P and Ti. It is speculated to be the volcanic debris, which is consistent with previous studies on plume particulate composition from the volcanic eruption of the NW Rota-1 volcano on the Mariana Arc and East Pacific Rise 9°50′N (Resing et al., 2007; Rouxel et al. 2016). Fig. 3c and 3d show the volcanic debris from Mata Fitu and East Mata (similar ones from Mata Fitu and West Mata not shown). It is worth noting that we did not find colloidal Fe-sulfides. However, the presence of Fe-sulfides in > 0.2 μm particulate fraction cannot be excluded.

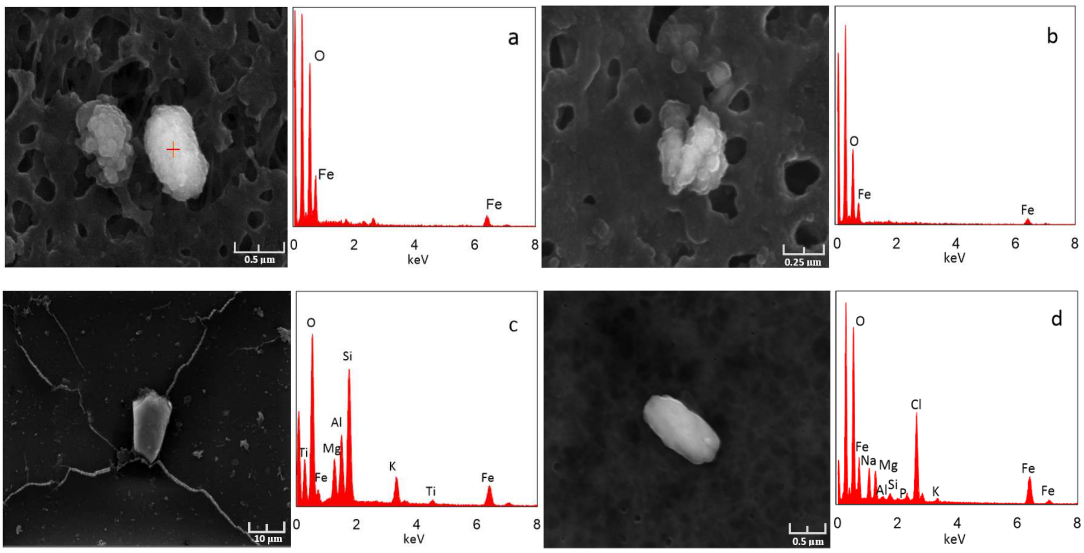

Fig. 3. a - d are SEM and EDX images of colloids of the hydrothermal samples from Mata Fitu (V6-2), West Mata (V13-24), Mata Ua (V9-8) and East Mata (V11-4), respectively. The multi-layer membrane (Millipore Co.) has a named pore size of 0.025 μm.

Table 1

Iron, Manganese and ligand concentrations and isotope compositions in hydrothermal plumes.

Sample ID	Water Depth (m)	pH_{sws}	tFe (nM)	dFe (nM)	dFe/tFe	δ^{56}tFe (‰)	2SD	δ^{56}dFe (‰)	2SD	tMn (nM)	dMn (nM)	$LogK'_{FeL}$	SD	L (nM)	SD	L/dFe
V6 samples (Mata Fitu)																
V6-16	1997.2	7.72	4.7	1.6	0.343	-0.47	0.10	0.85	0.08	8.0	n.a.	n.a.	n.a.	n.a.	n.a.	n.a.
V6-12	2397.0	7.71	7.1	4.1	0.574	-0.17	0.09	0.49	0.07	10.0	9.0	n.a.	n.a.	n.a.	n.a.	n.a.
V6-10	2436.1	7.68	148.5	86.1	0.580	-0.59	0.11	-1.69	0.07	131.1	n.a.	n.a.	n.a.	n.a.	n.a.	n.a.
V6-6	2483.9	7.70	36.6	20.8	0.569	-0.40	0.07	0.44	0.07	34.6	34.0	n.a.	n.a.	n.a.	n.a.	n.a.
V6-2	2549.5	7.68	156.1	64.2	0.411	-0.60	0.08	-1.5	0.06	158.5	154.3	n.a.	n.a.	n.a.	n.a.	n.a.
V9 samples (Mata Ua)																
V9-18	1600.1	7.76	6.2	4.4	0.714	-0.06	0.08	0.55	0.08	4.35	n.a.	21.4	0.15	3.28	0.03	0.75
V9-16	1960.7	7.76	5.0	2.8	0.559	0.27	0.24	0.31	0.09	4.8	n.a.	20.6	0.26	1.73	0.04	0.62
V9-14	2050.4	7.74	n.a.	5.3	n.a.	-0.30	0.14	-0.67	0.14	8.1	n.a.	n.a.	n.a.	n.a.	n.a.	n.a.
V9-12	2146.1	7.68	60.3	47.4	0.785	-0.70	0.05	-1.13	0.08	22.2	20.8	20.6	0.38	6.23	0.43	0.13
V9-8	2185.5	7.62	97.0	72.8	0.751	-0.48	0.06	-1.09	0.04	90.0	89.7	19.6	0.41	11.1	0.66	0.15
V9-6	2217.0	7.69	23.3	14.6	0.626	-0.56	0.02	-0.39	0.06	20.0	18.8	20.8	0.11	4.38	0.16	0.30
V9-4	2256.9	7.67	32.2	19.6	0.608	-0.12	0.08	-1.1	0.13	24.0	23.5	20.0	0.12	3.73	0.98	0.19
V9-2	2302.1	7.67	31.6	21.2	0.670	-0.64	0.07	-0.33	0.06	36.0	n.a.	20.5	0.23	6.09	0.34	0.29
V9-30	2334.4	7.68	26.8	15.5	0.578	-0.08	0.04	-0.28	0.08	25.4	23.5	20.2	0.05	5.19	0.17	0.33
V11 samples (East Mata)																
V11-14	900.7	7.77	7.2	5.6	0.778	n.a.	n.a.	0.31	0.17	8.3	n.a.	n.a.	n.a.	n.a.	n.a.	n.a.
V11-24	1001.8	7.76	7.6	5.4	0.710	-0.13	0.06	0.68	0.12	7.2	n.a.	n.a.	n.a.	n.a.	n.a.	n.a.
V11-12	1102.6	7.75	17.5	5.2	0.298	-0.07	0.06	0.10	0.06	14.5	12.3	n.a.	n.a.	n.a.	n.a.	n.a.

V11-10	1150.3	7.75	9.1	3.8	0.416	-0.68	0.06	0.14	0.07	10.2	8.6	n.a.	n.a.	n.a.	n.a.	n.a.
V11-8	1211.4	7.73	8.9	4.2	0.471	0.00	0.06	-0.44	0.09	7.6	8.2	n.a.	n.a.	n.a.	n.a.	n.a.
V11-6	1224.7	7.57	29.9	20.7	0.693	-0.01	0.06	0.33	0.05	27.5	25.7	n.a.	n.a.	n.a.	n.a.	n.a.
V11-4	1250.2	7.72	20.8	16.1	0.776	0.00	0.05	-0.42	0.08	12.1	10.6	n.a.	n.a.	n.a.	n.a.	n.a.
V11-2	1277.6	7.69	33.6	26.2	0.780	0.15	0.06	-0.45	0.06	17.9	16.0	n.a.	n.a.	n.a.	n.a.	n.a.
V13 samples (West Mata)																
V13-11	1101.4	7.74.	21.2	18.5	0.874	0.64	0.06	0.64	0.04	25.8	23.4	20.8	0.06	8.21	0.03	0.44
V13-21	1144.6	7.72.	67.0	27.8	0.415	0.25	0.05	n.a.	n.a.	30.5	n.a.	n.a.	n.a.	n.a.	n.a.	n.a.
V13-24	1228.5	7.72	65.3	16.3	0.250	0.28	0.02	-1.01	0.06	25.0	n.a.	19.7	0.07	4.12	0.38	0.25
V13-10	2201.2	7.73	12.1	6.4	0.528	0.06	0.05	-0.05	0.04	9.0	n.a.	20.7	0.08	3.08	0.37	0.48
V13-99	2325.4	7.73	26.0	5.8	0.223	0.51	0.30	0.24	0.06	13.0	12.1	21.0	0.13	3.25	0.08	0.56
V13-17	2501.3	7.72.	27.1	24.7	0.912	-0.09	0.05	0.3	0.04	13.0	12.6	20.7	0.11	8.81	0.08	0.36
V13-4	2649.3	7.72.	21.2	5.1	0.240	-0.04	0.07	0.54	0.13	11.0	n.a.	20.8	0.08	3.35	0.09	0.66

n.a.- not analyzed, pH_{sws} – pH on seawater scale, 2SD of Fe isotope measurements represent 2 standard deviation of either duplicate measurements or instrument precision, SD of $LogK'_{FeL}$ and L represent 1 standard deviation of duplicate measurements.

5. DISCUSSION

5.1. Isotope compositions of tFe

Total Fe includes both dissolved and particulate Fe. If there is no loss of Fe, tFe concentrations and isotope compositions should remain constant. However, for V6 and V9 samples collected over Mata Fitu and Mata Ua, δ^{56}tFe increases as tFe concentrations decrease with plume dispersal (Fig. 4a) suggesting the loss of isotopically light Fe from the plume. The precipitation of Fe-sulfides with a lighter Fe isotope composition is the likely explanation considering the high H_2S concentrations (3-9 mM) and low Fe/H_2S ratios (0.1-0.3) in the hydrothermal vent fluids from Mata Fitu and Mata Ua (Rubin et al., 2017, Table S1). Since we didn't observe the colloidal Fe-sulfides, the Fe sulfides or most Fe sulfides are assumed to be in the particulate phase (> 0.2 μm diameter). Similar variations in δ^{56}tFe were observed by Lough et al. (2017) at the East Scotia Ridge due to the precipitation of Fe-sulfides, although that was in a buoyant plume.

By contrast, δ^{56}tFe in V11 and V13 samples from East Mata and West Mata decreases as the plumes disperse, suggesting a loss of isotopically heavy Fe (Fig. 4b). This is likely related to the precipitation of isotopiecally heavier Fe-oxyhydroxides which results in lighter Fe isotopes being retained in the dissolved phase. The formation of Fe-oxyhydroxides instead of Fe-sulfides in V13 samples derived from West Mata is consistent with the low H_2S concentrations (~0.1 mM) and high Fe/H_2S ratio (~7.28) in hydrothermal fluids (Rubin et al., 2017, Table S1). It has been well shown that the hydrothermal system at West Mata was dominated by the discharge of magmatic volatiles containing high concentrations of SO_2, H_2 and CO_2 (Embley et al., 2006; Butterfield et al., 2011; Resing et al., 2011; de Ronde and Stucker, 2015; Walker et al., 2019). Volcanic SO_2 reacts with water and forms sulfurous and sulfuric acid and elemental S (reaction 2 and 3). H_2S can be removed by oxidation (reaction 4), thus leading to low H_2S concentrations in hydrothermal fluids and plumes. This is very different from water/rock-dominated hydrothermal systems on Mid-Ocean

Ridges, which is enriched with high concentrations of H_2S.

$$3SO_2 + 2H_2O = S_{(s)} + 2H_2SO_4 \quad (2)$$

$$SO_2 + H_2O = HSO_3^- + H^+ \quad (3)$$

$$2H_2S + SO_2 = 3S_{(s)} + 2H_2O \quad (4)$$

So far, no vent fluids have been collected at East Mata. Considering the similar shape, size and CH_4 and H_2 concentrations with West Mata (Rubin et al., 2017) and that East Mata is dominated with low-temperature hydrothermal venting (Baker et al., 2019), we speculate that V11 plume samples over East Mata have similar chemical characteristics with V13 samples from West Mata. In future, more investigations are need to confirm this assumption.

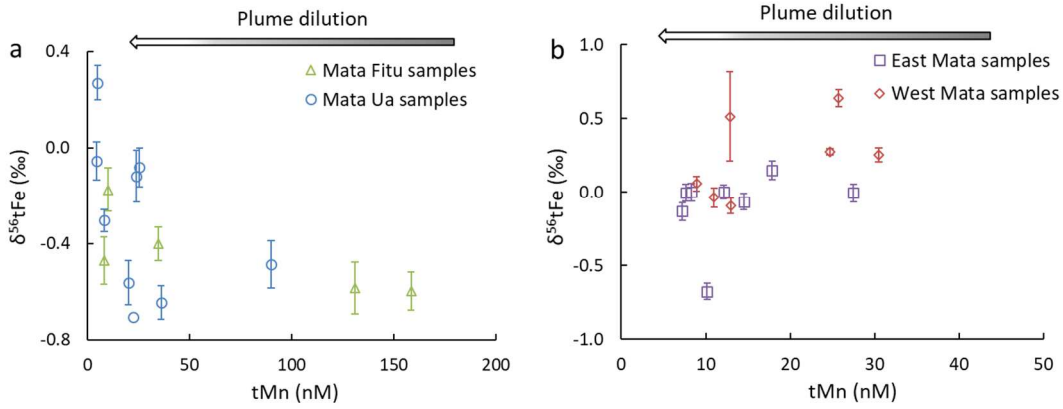

Fig. 4. tFe isotope compositions of Mata Fitu and Mata Ua during the hydrothermal plume dispersal (a). tFe isotope compositions of East Mata and West Mata during the hydrothermal plume dispersal (b). tMn was used as the near conservative tracer of plume dilution. The error bars represent ± 2 standard deviation of either duplicate measurements or instrument precision.

5.2. The dissolved Fe isotope composition

In the non-buoyant plume, the formation of particulate Fe-oxyhydroxides should be the dominant process transforming dFe and this process would leave the dissolved fraction isotopically lighter. However, δ^{56}dFe of all four plumes show increasingly heavier isotopes with progressing plume dilution except two samples from West Mata and East Mata (Fig. 5a and 5b). One possible explanation for the increase of δ^{56}dFe is that a proportion of the "particulate" Fe-oxyhydroxides exists in the colloidal phase. This heavy "particulate" or colloidal phase passes through the 0.2 μm filter thus

reducing the loss of isotopically heavy Fe from the dissolved phase. This is confirmed by the SEM images and EDX analysis (Fig. 3). Although we did not measure the colloidal Fe concentrations, previous investigations have revealed variable high percentages of colloidal Fe is in the dFe (5~96%) pool within hydrothermal plumes (Sands et al., 2012; Hawkes et al., 2013a; Fitzisimmons et al., 2015; Wang et al., 2019). However, it still cannot explain the increasing trend of δ^{56}dFe as the hydrothermal plume disperses. A reasonable explanation is that a proportion of hydrothermal Fe is bound with organic ligands, which favors reaction with heavy Fe isotopes (Dideriksen et al., 2008; Horner et al., 2015; Morgan et al., 2010). Recently, more studies have shown that high concentrations of organically bound Fe can occur in a hydrothermal plume, which can stabilize the Fe in the dissolved phase (Bennett et al., 2008; Hawkes et al., 2013a; Kleint et al., 2016; Wang et al., 2019, 2021a). Hawkes et al. (2013a) and Wang et al. (2019, 2021a) suggested that ~30% of dFe is as organic Fe complexes. Moreover, Kleint et al. (2016) found that Fe-binding ligand concentrations can be more than 3 μM in buoyant plumes.

Fitzsimmons et al. (2016, 2017) found δ^{56}dFe > 0.5‰ more than 1,000 km from their venting sites. Organically complexed Fe and colloidal Fe-oxyhydroxides could contribute heavy δ^{56}dFe observed by Fitzsimmons and coworkers. In non-buoyant plume samples collected near venting sites along the Scotia Arc (Klar et al., 2017) and Vanuatu back Arc (Nasemann et al., 2018), δ^{56}dFe increased with plume dispersion, similar to the trend observed here. However, δ^{56}dFe values observed here are significantly heavier than those observed in either the Scotia Arc (< -0.21‰) or Vanuatu back Arc (< -0.16‰); hence, there might be additional factors influencing the δ^{56}dFe signal. Volcanic eruptions and magmatic-hydrothermal venting result in large inputs of CO_2 and SO_2 into the hydrothermal system and decreases in pH in hydrothermal plumes (Resing et al., 2007, 2009, 2011; de Ronde and Stucker, 2015). Except the flank of West Mata samples, the other three plume samples had pH values ranging from 7.57 to 7.77 (Table 1), which were lower than the ambient

seawater (~ 7.80, Resing et al., 2011). Moreover, a CTD tow along the spine of West Mata detected lower pH values of < 7.40 in hydrothermal plumes (data not shown). This decreases in pH result in decreases in both Fe(II) oxidation rates and Fe(III) hydrolysis, thus reducing the loss of particulate Fe-oxyhydroxides with heavy δ^{56}Fe.

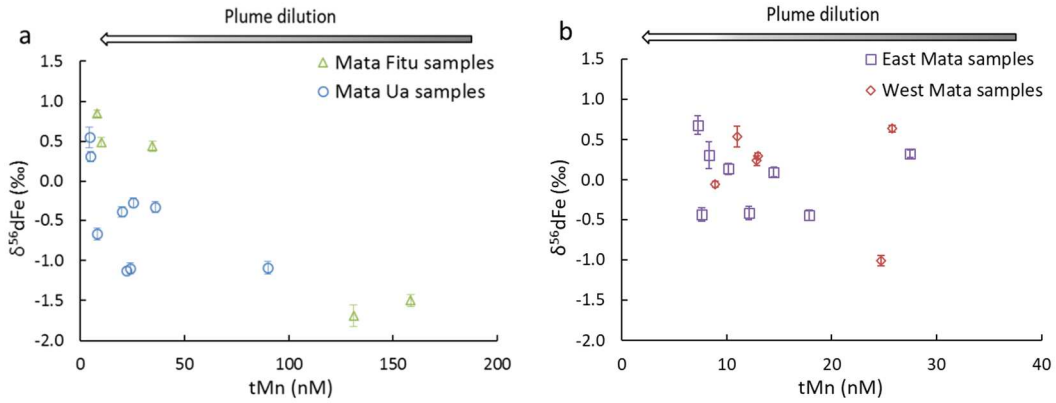

Fig. 5. dFe isotope composition during the hydrothermal plume dispersal. The error bars represent ± 2 standard deviation of either duplicate measurements or instrument precision..

5.3. Characterisation of Fe ligands and their relationship to Fe isotopes

The organic ligand concentrations measured in Mata Ua and West Mata plume samples are comparatively higher than in background seawater (about 1-2 nmol/L, see Gledhill and Buck, 2012 for a review), and positively related to dFe concentrations (Fig. S1a), which might indicatea hydrothermal source for these ligands. In addition, observed ligand concentrations are consistently lower than dFe which is in contrast to background seawater where ligands tend to be in excess of dFe. The percentage of ligand-bound Fe in dFe ranged between 13% and 75%, and averaged 35 ± 22% for Mata Ua and 46 ± 14% for West Mata. Similar values have been observed in hydrothermal plumes over the East Scotia Ridge (25 ± 15% at E2 vent and 39 ± 27% at E9N vent, Hawkes et al., 2013a), Southwest Indian Ridge (29 ± 8% at Dragon Flag vent, Wang et al., 2019) and South Mariana Back-arc (29 ± 9%, Wang et al., 2021a). Ratios of L/dFe negatively correlate with tMn (Fig. S1b) suggesting an increase of the ligands compared with dFe. The precipitation of colloidal Fe oxyhydroxides and sulfides might be a possible reason, and microbial carbon production in hydrothermal plumes might be another possible source of the higher ligand concentrations (Wang et al., 2021a).

However, it should be noted that CLE-ACSV is an operationally-defined method. The determined $\log K'_{FeL}$ and L are dependent on the added competing ligand and its

concentrations and the associated data treatments. They represent the average values of multiple Fe-binding ligands present in any given sample (Gledhill and Buck, 2012). Moreover there might be interdependencies between L, logK and dFe. The high dFe results in high L and low $\log K'_{FeL}$, considering that the stronger ligands are complexed first at low concentration of dFe, and the comparatively weaker ligands would be available for complexation at high dFe concentration (Town and Filella, 2000; Gledhill and Gerringa, 2017). More recently, it has been suggested that binding site heterogeneity (i.e. the distribution of binding site strengths) is another critical factor for the interpretation of Fe binding in marine systems (Lodeiro et al., 2021; Zhu et al., 2021; Gledhill et al., 2022). The correlation between dFe and L might therefore reflect the assumption that there is only one ligand rather than many binding sites with varying strength (Town and Filella, 2000; Gledhill and Gerringa, 2017), a factor we were not able to address in this study. Future studies combining the CLE-ACSV method and Non-Ideal Competitive Adsorption (NICA)-Donnan model can improve the understanding of Fe speciation data (Zhu et al., 2021).

The conditional stability constant for FeL complexes is positively correlated with δ^{56}dFe ($r^2 = 0.6$, $p < 0.001$, Fig. 6a), indicating that stronger ligands or binding sites lead to heavy δ^{56}dFe. This suggests that the fractionation factor between organic and inorganic Fe, $\alpha_{FeL\text{-}Fe(III)}$, increases with ligand binding strength. This observation is supported by the experimental results obtained by Dideriksen et al. (2008) and Morgan et al. (2010) for isotope fractionation increasing with Fe-ligand binding strength. To our knowledge, this study is the first investigation of the effect of organic binding on Fe isotope fractionation in field samples. Noteworthy, there is no correlation between ligand concentration and δ^{56}dFe (Fig. 6b), indicating the $\alpha_{FeL\text{-}Fe(III)}$ depends on the ligand binding strength and not the concentration of Fe binding ligands. However, it should be noted that the ligands determined here don't include those ligands which cannot compete with 1N2N. More studies are needed to verify these relationships.

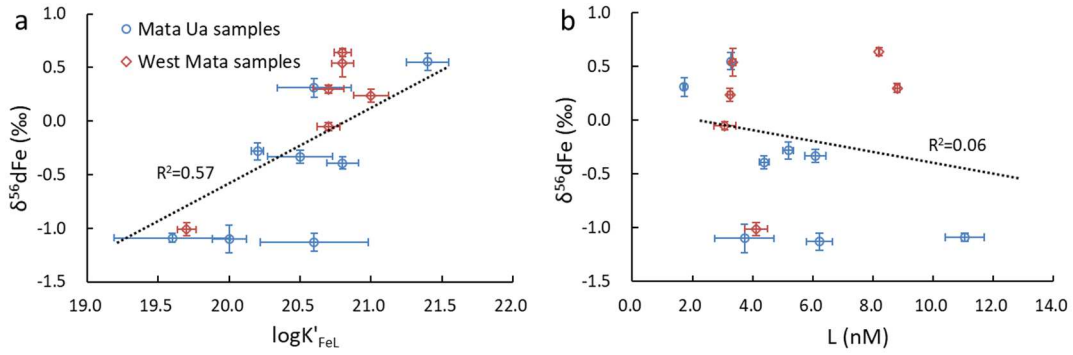

Fig. 6. The relationships between $\log K'_{FeL}$ and δ^{56}dFe (a), L and δ^{56}dFe (b). The error bars on $\log K'_{FeL}$ and L represent ±1 standard deviation of two replicate measurement.

5.4. Dissolved Fe isotope-fractionation in hydrothermal plumes

We built a model to describe the evolution of dissolved Fe isotopic in different chemical processes during mixing of hydrothermal fluids with ambient seawater. It is well known that Rayleigh distillation models can be used to depict isotope ratios in a homogeneous reservoir from which a phase is continuously removed (Broecker and Oversby, 1971; Rayleigh, 1896). Here, we model the effects of Fe-sulfides (FeS_2) and –oxyhydroxides (FeOOH) formation and removal, organic complexation and colloidal Fe-oxyhydroxides on Fe isotope fractionation in the Mata Ua and West Mata plumes. These processes labelled with ①, ②, ③ and ④ can be described as follows:

$$Fe(II)_{VF} \xrightarrow{①} Fe(II)_{\text{-}FeS2} \xrightarrow{②} Fe(III) \begin{cases} \xrightarrow{③} FeL \\ \xrightarrow{④} FeOOH\ (nano+particulate) \end{cases}$$

The process ① describes the partial precipitation and removal of dFe as Fe-sulfides. The δ^{56}Fe of the remaining dFe pool ($\delta^{56}Fe_{_S_2}$) can be estimated using a Rayleigh fractionation model (Eq. (5)).

$$\delta^{56}Fe_{\_S_2} = (\delta^{56}Fe_V + 1000) \cdot f^{\alpha-1} - 1000 \qquad (5)$$

where $\delta^{56}Fe_{VF}$ is the Fe isotope composition of the end-member vent fluid (-0.54‰ and 0.13‰ for Mata Ua and West Mata fluids, respectively), α is the fractionation factor between FeS_2 and Fe(II) (~0.9992) taken from Butler et al. (2005), f is the fraction of the remaining Fe in the dissolved phase after FeS_2 formation and is related to the Fe/H_2S ratio in hydrothermal fluid. Previous work has shown that ~30% of the hydrothermal Fe is precipitated as FeS_2 when Fe/H_2S = 0.2 (Lough et al., 2017), and ~

4% is precipitated as FeS_2 with Fe/H_2S = 24 (Severmann et al., 2004). Accordingly, for Mata Ua samples, we assumed 30% of the hydrothermal Fe was FeS_2 (f = 0.7) given that Fe/H_2S ratio is 0.1-0.3 in the hydrothermal fluids at Mata Fitu. For West Mata samples, 13% was assumed to be the FeS_2 (f = 0.87) considering that Fe/H_2S is ~ 7.28. Based on these two factors, $\delta^{56}Fe_{-S_2}$ were calculated to be -0.25‰ and 0.24‰ for Mata Ua and West Mata plume samples, respectively, using Eq. (5).

Following the formation of FeS_2, a portion of the remaining Fe(II) is likely to be oxidized to Fe(III) described as process ② and it can be modeled as a Rayleigh fractionation process using Eqs. (6) and (7).

$$\delta^{56}Fe(II) = (\delta^{56}Fe_{-S_2} + 1000) \cdot F_1^{\alpha_1 - 1} - 1000 \quad (6)$$

$$\delta^{56}Fe(III) = (\delta^{56}Fe_{-S_2} + 1000) \cdot \frac{1 - \alpha_1}{1 - } - 1000 \quad (7)$$

Where $\delta^{56}Fe(II)$ is the isotopic composition of the remaining Fe(II), $\delta^{56}Fe(III)$ is the isotopic composition of the newly formed Fe(III), α_1 is the fractionation factor between aqueous Fe(II) and Fe(III), which is ~1.0036 based on Welch et al. (2013). F_1 is the proportion of remaining Fe(II) after Fe(II) oxidised to $\delta^{56}Fe(III)$, which is related to the Fe(II) oxidation rate. Fe(II) oxidation process is shown to be pseudo-first-order with respect to the Fe(II) concentration (Millero et al., 1987; King, 1998). The Fe(II) half-life depends on solution pH and dissolved O_2 concentration. The calculated mean half-lives for Mata Ua and flank of West Mata samples are 3.2 ± 0.7 and 2.7 ± 0.2 h, respectively (see Appendix). The CTD recovery time and the delay of ~ 4 h between sampling and filtration of the Mata Ua correspond to ~1.3 $t_{1/2}$. The time for plume dispersal of West Mata (~ 13.8 h) and the delay time between sampling and filtration (~ 4 h) correspond to roughly 6.6 $t_{1/2}$. As a result, F_1 values are 0.41 and 0.01 for Mata Ua and West Mata samples, respectively.

Process ③ is that the forming Fe(III) is partially complexed by organic ligands to form FeL. $\delta^{56}Fe$ of the formed FeL ($\delta^{56}FeL$) and left Fe(III) ($\delta^{56}Fe(III)'$) can be modelled using Eq (8) and (9).

$$\delta^{56}Fe(III)' = (\delta^{56}Fe(III) + 1000) \cdot F_2^{\alpha_2 - 1} - 1000 \quad (8)$$

$$\delta^{56}FeL = (\delta^{56}Fe(III) + 1000) \cdot \frac{1 - \alpha_2}{1 - {}_2} - 1000 \quad (9)$$

Where F_2 is the proportion of remaining Fe(III) after FeL formation. α_2 is the fractionation factor of 1.0006 between FeL and Fe(III) based on Dideriksen et al. (2008), which indicated that the fractionation of the iron isotopes between FeL and Fe(III) ($\Delta^{56}Fe_{FeL\text{-}Fe(III)}$) is 0.60 ± 0.15‰, depending on Fe-binding affinity of the organic ligands.

The remaining Fe(III), Fe(III)′, is precipitated as particulate FeOOH and colloidal (nano-scale) FeOOH ($FeOOH_{nano}$), which is the process ④. Because this process is very fast, there is no or very limited isotope fractionation between Fe(III) and FeOOH (Welch et al., 2003; Kappler et al., 2010; Wu et al., 2011; Wang et al., 2021b). However, the formed particulate FeOOH would be removed from the dissolved phase and thus alter the δ^{56}dFe. The fraction of FeL (F_{FeL}) in dFe including FeL, $FeOOH_{nano}$ and the remaining Fe(II) can be depicted using Eq (10). Accordingly, the δ^{56}dFe delivered to the plume can be calculated using a mass balance approach incorporating δ^{56}FeL, $\delta^{56}FeOOH_{nano}$ and δ^{56}Fe(II), which is described using Eq (11).

$$F_{L} = \frac{FeL}{Fe(II) + FeL + FeOOH_{nano}} = \frac{(1 - F_1) \cdot (1 - F_2)}{F_1 + (1 - F_1) \cdot (1 - F_2) + (1 - F_1) \cdot F_2 \cdot X} \quad (10)$$

$$\delta^{56}dFe = \delta^{56}Fe(II) \cdot F_{(II)} + \delta^{56}Fe_{L} \cdot F_{L} + \delta^{56}FeOOH_{nano} \cdot F_{OOH}$$

$$= \frac{F_1 \cdot \delta^{56}Fe(II) + (1 - F_1) \cdot (1 - F_2) \cdot \delta^{56}Fe_{L} + (1 - F_1) \cdot F_2 \cdot X \cdot \delta^{56}FeOOH_{nano}}{F_1 + (1 - F_1) \cdot (1 - F_2) + (1 - F_1) \cdot F_2 \cdot X} \quad (11)$$

Where $F_{Fe(II)}$, F_{FeL} and $F_{FeOOHnano}$ are the fractions of Fe(II) , FeL and $FeOOH_{nano}$ in dFe respectively, $\delta^{56}FeOOH_{nano}$ is the isotopic composition of the nano FeOOH, which equals to that of the remaining Fe(III) (δ^{56}Fe(III)′), X is the proportion of the $FeOOH_{nano}$ in the formed FeOOH (particulate FeOOH + nano FeOOH).

Fig. 7a and 7b show the evolution of δ^{56}dFe as a function of F_{FeL} and the proportion of removed particulate FeOOH (1-X) in the Mata Ua and West Mata plume samples. It suggests that this model well describes the δ^{56}dFe evolution in the above four processes during mixing of hydrothermal fluids with ambient seawater and forming buoyant and non-buoyant plumes. The model fit for Mata Ua samples is when no

more than 65% FeOOH is removed from the dissolved phase as particulate Fe. Comparatively, for West Mata samples, the best model fits when less than 93% FeOOH is removed from the dissolved phase. The difference may be related to the plume dispersal time and distance, which affect the aggregation and precipitation of nano FeOOH. These results are reasonable and also consistent with previous observations that 5 ~ 96% of dFe is present as colloidal Fe in hydrothermal plumes (Sands et al., 2012; Hawkes et al., 2013a; Fitzsimmons et al., 2014; Wang et al., 2019).

It is noteworthy that the δ^{56}dFe of two Mata Ua samples and two West Mata are heavier than the predicted values, although there is no significant difference between them. Moreover, those two Mata Ua samples have higher fractions of FeL in dFe (F_{FeL}) than the predicted F_{FeL}. We speculate that the likely reason is the Fe(II) complexation with organic ligands, which were not included in our model. The formation of organic Fe(II) complexes might favour heavier δ^{56}dFe in dFe similar to Fe(III), and lead to higher ligand concentrations. Another reason might be related to the use of inappropriate parameters such as the fraction of hydrothermal Fe precipitated as Fe sulfides and the calculation of Fe(II) oxidation half-lives.

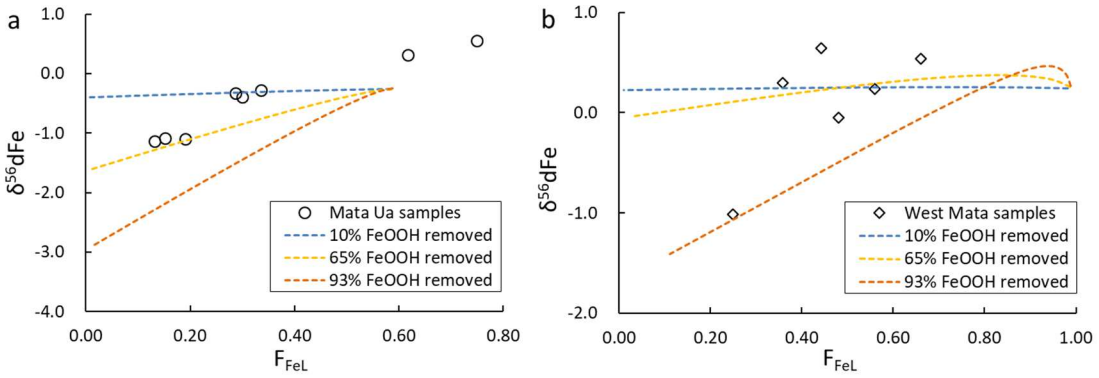

Fig. 7. The fitting of δ^{56}dFe with the fraction of FeL in dFe (F_{FeL}) in the hydrothermal plumes at Mata Ua (V9) (a) and West Mata (V13) (b).

6. CONCLUSION

We investigated the total and dissolved Fe composition (δ^{56}tFe, δ^{56}dFe) and organic

ligand-bound Fe characteristics in the hydrothermal plumes over arc volcanoes in the Northeast Lau Basin. The results show δ^{56}tFe and δ^{56}dFe are influenced by the vent fluid chemistry. Due to the difference in H_2S concentrations and Fe/H_2S ratios in the hydrothermal fluids, δ^{56}tFe might show an increasing or decreasing trend with plume dispersal. However, the δ^{56}dFe increase to as high as 0.85‰ with progressing plume dilution, which suggests submarine hydrothermal systems at arc volcanes can export significantly heavier δ^{56}dFe than the previously reported δ^{56}dFe in other hydrothermal systems.

Iron binding ligands ([L] or FeL) constitute 35 ± 22% and 46 ± 14% of the dFe pool in Mata Ua and flank of West Mata plume samples. We observed a positive relationship between K'_{FeL} and δ^{56}dFe, which confirms that the stronger FeL complexes lead to the enrichment of heavy Fe isotope composition of δ^{56}dFe. However, there is no direct relationship between δ^{56}dFe and ligand concentrations. The input of magmatic CO_2 and SO_2 from volcanic arc into the hydrothermal plumes might lead to comparatively lower pH and hence decrease Fe(II) oxidation rate and Fe(III) hydrolysis , and thus reduce the loss of particulate Fe-oxyhydroxides with heavy δ^{56}Fe.

To predict the δ^{56}dFe during plume dispersal, we propose a Rayleigh distillation model utilizing a mass balance approach incorporating FeL, nano-scale FeOOH and remaining Fe(II). The δ^{56}dFe of both Mata Ua and West Mata samples are well described by this model, which indicates the importance of organic Fe complexation and colloidal FeOOH on the dissolved Fe isotope composition. For future studies we recommend investigation of Fe(II) complexation with organic ligands and its effect on Fe isotope fractionation in hydrothermal settings.

ACKNOWLEDGEMENT

The authors thank chief scientist Ken Rubin and all the participants and crew of the R/V Falkor for the FK171110 cruise. We thank the Schmidt Ocean Institute for providing the ship time

aboard the RV Falkor. We thank Sharon Walker for CTD data, especially for Oxidation Reduction Potential and Light Scattering Sensor data. We thank Susan Merle for providing maps and GIS support. We would also like to thank the editor and two anonymous reviewers whose comments improved the quality of this manuscript. This work was supported by National Natural Science Foundation of China (No. 42076062, 41376048). The seagoing program was funded by NOAA's Ocean Exploration and Research and the Pacific Marine Environmental Laboratory's (PMEL) Earth Ocean Interactions program through the Cooperative Institute for Climate, Ocean, & Ecosystem Studies. This is PMEL publication #5360 and CICOES # 2022-1183).

REFERENCES

Archer D. E. and Johnson K. (2000) A model of the iron cycle in the ocean. *Glob.Biogeochem.Cyc.* **14**, 269-279.

Baker E. T., Walker S. L., Massoth G. J. and Resing J. A. (2019) The NE Lau Basin: Widespread and Abundant Hydrothermal Venting in the Back-Arc Region Behind a Superfast Subduction Zone. *Front. Mar. Sci.* **6**, 382.

Baumberger T., Lilley M. D., Resing J. A., Lupton J. E., Baker E. T., Butterfield D. A., Olson E. J. and Früh-Green, G. L. (2014) Understanding a submarine eruption through time series hydrothermal plume sampling of dissolved and particulate constituents: West Mata, 2008–2012. *Geochem. Geophys. Geosyst.* **15**, 4631-4650.

Bennett S. A., Achterberg E. P., Connelly D. P., Statham P. J., Fones G. R. and German C. R. (2008) The distribution and stabilisation of dissolved Fe in deep-sea hydrothermal plumes. *Earth Planet. Sci. Lett.* **270**, 157-167.

Bennett S. A., Rouxel O., Schmidt K., Nberg D. G., Statham P. J. and German C. R. (2009) Iron isotope fractionation in a buoyant hydrothermal plume, 5 degrees S Mid-Atlantic Ridge. *Geochim. Cosmochim. Acta* **73**, 5619-5634.

Bennett S. A., Hansman R. L., Sessions A. L., Nakamura K. I. and Edwards K. J. (2011) Tracing iron-fueled microbial carbon production within the hydrothermal plume at the Loihi seamount. *Geochim. Cosmochim. Acta* **75**, 5526-5539.

623 Bevis M., Taylor F. W., Schutz B. E., Recy J., Isacks B. L., Helu S., Singh R., Kendrick E.,
624 Stowell J., Taylor B. and Calmantli S. (1995) Geodetic observations of very rapid convergence
625 and backarc extension at the Tonga arc. *Nature* **374**, 249-251.
626 Boyd P. W., Ellwood M. J., Tagliabue A. and Twining B. S. (2017) Biotic and abiotic retention,
627 recycling and remineralization of metals in the ocean. *Nat. Geosci*. **10**, 167-173.
628 Boyd P. W., Watson A. J., Law C. S., Abraham E. R., Trull T., Murdoch R., Bakker D. C. E.,
629 Bowie A. R., Buesseler K. O., Chang H., Charette M., Croot P., Downing K., Frew R., Gall M.,
630 Hadfield M., Hall J., Harvey M., Jameson G., LaRoche J., Liddicoat M., Ling R., Maldonado
631 M. T., McKay R. M., Nodder S., Pickmere S., Pridmore R., Rintoul S., Safi K., Sutton P.,
632 Strzepek R., Tanneberger K., Turner S., Waite A. and Zeldis J. (2000) A mesoscale
633 phytoplankton bloom in the polar Southern Ocean stimulated by iron fertilization. *Nature* **407**,
634 695-702.
635 Broecker W. S. and Oversby V. M. (1971) Chemical equilibria in the earth. *Mcgraw-Hill, New*
636 *York* **318**, 165-167.
637 Buck K. N., Sohst B. and Sedwick P. N. (2015) The organic complexation of dissolved iron along
638 the U.S. GEOTRACES (GA03) North Atlantic Section. *Deep-Sea Res. II* **116**, 152-165.
639 Bullen T. D., White A. F., Childs C. W., Vivit D. V. and Schulz M. S. (2001) Demonstration of
640 significant abiotic iron isotope fractionation in nature. *Geology* **29**, 699-702.
641 Butler I. B., Archer C., Vance D., Oldroyd A. and Rickard D. (2005) Fe isotope fractionation on
642 FeS formation in ambient aqueous solution. *Earth Planet. Sci. Lett.* **236**, 430-442.
643 Butterfield D. A., Nakamura K. I., Takano B., Lilley M. D., Lupton J. E., Resing J. A. and Roe K.
644 K. (2011) High SO_2 flux, sulfur accumulation, and gas fractionation at an erupting submarine
645 volcano. *Geology* **39**, 803-806.
646 Conway T. M. and John S. G. (2014) Quantification of dissolved iron sources to the North
647 Atlantic Ocean. *Nature* **511**, 212-215.
648 de Ronde C. E. J., Baker E. T., Massoth G. J., Lupton J. E., Wright I. C., Sparks R. J., Bannister S.
649 C., Reyners M. E., Walker S. L., Greene R.R., Ishibashi J., Faure K., Resing J. A., Lebon G.T.
650 (2007) Submarine hydrothermal activity along the mid-Kermadec Arc, New Zealand:

Large-scale effects on venting. *Geochem. Geophys. Geosyst.* **8**, 1525-2027.

de Ronde C. E. J. and Stucker V. K. (2015) Seafloor hydrothermal venting at volcanic arcs and backarcs. In *The Encyclopedia of Volcanoes* (eds. H. Sigurdsson, B. Houghton, S. McNutt, H. Rymer and J. Stix). Academic Press Elsevier, pp. 823-849.

Douville E., Charlou J. L., Oelkers E. H., Bienvenu P., Colon C. F.J., Donval J. P., Fouquet Y., Prieur D. and Appriou P. (2002) The rainbow vent fluids (36 degrees 14 ′ N, MAR): the influence of ultramafic rocks and phase separation on trace metal content in Mid-Atlantic Ridge hydrothermal fluids. *Chem. Geol.* **184**, 37-48.

Dideriksen K., Baker J. A. and Stipp S. L. S. (2006) Iron isotopes in natural carbonate minerals determined by MC-ICP-MS with a ^{58}Fe-^{54}Fe double spike. *Geochim. Cosmochim. Acta* **70**, 118-132.

Dideriksen K., Baker J. A. and Stipp S. L. S. (2008) Equilibrium Fe isotope fractionation between inorganic aqueous Fe(III) and the siderophore complex, Fe(III)-desferrioxamine B. *Earth Planet. Sci. Lett.* **269**, 280-290.

Domagal-Goldman S. D., Paul K. W., Sparks D. L. and Kubicki J. D. (2009) Quantum chemical study of the Fe(III)-desferrioxamine B siderophore complexsElectronic structure, vibrational frequencies, and equilibrium Fe-isotope fractionation. *Geochim. Cosmochim. Acta* **73**, 1-12.

Ellwood M. J., Hutchins D. A., Lohan M. C., Milne A. , Nasemann P., Nodder S. D., Sander S. G., Strzepek R., Wilhelm S. W. and Boyd (2015) Iron stable isotopes track pelagic iron cycling during a subtropical phytoplankton bloom. *Proc. Natl. Acad. Sci. U.S.A.* **112**, E15-E20.

Ellwood M. J., Strzepek R. F., Strutton P. G., Trull T. W. and Boyd P. W. (2020) Distinct iron cycling in a Southern Ocean eddy. *Nat. Commun.* **11,** 825.

Embley R. W., Chadwick W. W., Baker E. T., Butterfield D. A., Resing J. A., de Ronde C. E. J., Tunnicliffe V., Lupton J. E., Juniper S. K. and Rubin K. H., et al. (2006) Long-term eruptive activity at a submarine arc volcano. *Nature* **441**, 494-497.

Field M. P. and Sherrell R. M. (2000) Dissolved and particulate Fe in a hydrothermal plume at 9°45’ N, East Pacific Rise: slow Fe(II) oxidation kinetics in Pacific plumes. *Geochim. Cosmochim. Acta* **64**, 619-628.

679 Findlay A. J., Gartman A., Shaw T. J. and Luther G. W. (2015) Trace metal concentration and
680 partitioning in the first 1.5m of hydrothermal vent plumes along the Mid-Atlantic Ridge: TAG,
681 Snakepit, and Rainbow. *Chem. Geol.* **412**, 117-131.
682 Fitzsimmons J. N., Boyle E. A. and Jenkins W. J. (2014) Distal transport of dissolved
683 hydrothermal iron in the deep South Pacific Ocean. *Proc. Natl. Acad. Sci. U.S.A.* **111**,
684 16654-16661.
685 Fitzsimmons J. N., Carrasco G. G., Wu, J., Roshan S. and Boyle E. A. (2015) Partitioning of
686 dissolved iron and iron isotopes into soluble and colloidal phases along the ga03 geotraces
687 north atlantic transect. *Deep-Sea Res. II* **116**, 130-151.
688 Fitzsimmons J. N., Conway T. M., Lee J. M., Kayser R., Thyng K. M., John S. G. and Boyle E. A.
689 (2016) Dissolved iron and iron isotopes in the southeastern Pacific Ocean. *Glob. Biogeochem.*
690 *Cycl.* **30**, 1372-1395.
691 Fitzsimmons J. N., John S. G., Marsay C. M., Hoffman C. L., Nicholas S., Toner B. M., German
692 C. R. and Sherrell R. M. (2017) Iron persistence in a distal hydrothermal plume supported by
693 dissolved–particulate exchange. *Nat. Geosci.* **10**, 195-201.
694 Gartman A., Findlay A. J. and Luther G. W. (2014) Nanoparticulate pyrite and other nanoparticles
695 are a widespread component of hydrothermal vent black smoker emissions. *Chem. Geol.* **366**,
696 32-41
697 German C. R., Casciotti K. A., Dutay J. C., Heimbu¨rger L. E., Jenkins W. J., Measures C. I.,
698 Mills R. A., Obata H., Schlitzer R., Tagliabue A., Turner D. R. and Whitby H. (2016)
699 Hydrothermal impacts on trace element and isotope ocean biogeochemistry. *Phil. Trans. R. Soc.*
700 *A* **374,** 20160035.
701 Gledhill M. and Buck K. N. (2012) The organic complexation of iron in the marine environment:a
702 review. *Front. Microbiol.* **3**, 1-17.
703 Gledhill M. and Gerringa L. J. A. (2017). The effect of metal concentration on the parameters
704 derived from complexometric titrations of trace elements in seawater—a model study. *Front.*
705 *Mar. Sci.*, **4**, 254.
706 Gledhill M., Zhu K., Rusiecka D. and Achterberg E. P. (2022) Competitive interactions between

707 microbial siderophores and Humic-Like binding sites in european shelf sea waters. *Front. Mar.*
708 *Sci.* **9**, 595.
709 Hawkes J. A., Connelly D. P., Gledhill M. and Achterberg E. P. (2013a) The stabilisation and
710 transportation of dissolved iron from high temperature hydrothermal vent systems. *Earth*
711 *Planet. Sci. Lett.* **375**, 280-290.
712 Hawkes J. A., Gledhill M., Connelly D. P. and Achterberg E. P. (2013b) Characterisation of iron
713 binding ligands in seawater by reverse titration. *Anal. Chim. Acta* **766**, 53 – 60.
714 Horner T. J., Williams H. M., Hein J. R., Saito M. A., Burton K. W., Halliday A. N. and Nielsen S.
715 G. (2015) Persistence of deeply sourced iron in the Pacific Ocean. *Proc. Natl. Acad. Sci. U.S.A.*
716 **112**, 1292-1297.
717 James R. H. and Elderfield H. (1996) Dissolved and particulate trace metals in hydrothermal
718 plumes at the Mid-Atlantic Ridge. *Geophys. Res. Lett.* **23**, 3499-3502.
719 Kappler A., Johnson C. M., Crosby H. A., Beard B. L. and Newman D. K. (2010) Evidence for
720 equilibrium iron isotope fractionation by nitrate-reducing iron(II)-oxidizing bacteria. *Geochim.*
721 *Cosmochim. Acta* **74**, 2826–2842.
722 King D. W. (1998) Role of carbonate speciation on the oxidation rate of Fe(II) in aquatic systems.
723 *Environ. Sci. Technol.* **32**, 2997-3003.
724 Klar J. K., James R. H., Gibbs D., Lough A., Parkinson I., Milton J. A., Hawkes J. A. and
725 Connelly D. P. (2017) Isotopic signature of dissolved iron delivered to the Southern Ocean
726 from hydrothermal vents in the east Scotia Sea. *Geology (Boulder)* **45**, 351-354.
727 Kleint C., Hawkes J. A., Sander S. G. and Koschinsky A. (2016) Voltammetric investigation of
728 hydrothermal iron speciation. *Front. Mar. Sci.* **3**, 75.
729 Kleint C., Zitoun R., Neuholz R., Walter M., Schnetger B., Klose L., Chiswell S. M., Middag R.,
730 Laan P., Sander S. G. and Koschinsky A. (2022) Trace metal dynamics in shallow
731 hydrothermal plumes at the Kermadec arc. *Front. Mar. Sci.* **8**, 782734.
732 Lang S. Q., Butterfield D. A., Lilley M. D., Johnson H. P. and Hedges J. I. (2006) Dissolved
733 organic carbon in ridge-axis and ridge-flank hydrothermal systems. *Geochim. Cosmochim.*
734 *Acta* **70**, 3830-3842.

735 Lodeiro P., Rey-Castro C., David C., Puy J., Achterberg E. P. and Gledhill M. (2021) Seasonal
736 variations in proton binding characteristics of dissolved organic matter isolated from the
737 Southwest Baltic Sea. *Environ. Sci. Technol.* **55**, 16215-16223.
738 Lough A. J. M., Klar J. K., Homoky W. B., Comer-Warner S. A., Milton J. A., Connelly D. P.,
739 James R. H. and Mills R. A. (2017) Opposing authigenic controls on the isotopic signature of
740 dissolved iron in hydrothermal plumes. *Geochim. Cosmochim. Acta* **202**, 1-20.
741 Millero F. J., Sotolongo S. and Izaguirre M. (1987) The oxidation kinetics of Fe(II) in seawater.
742 *Geochim. Cosmochim. Acta* **51**, 793-801.
743 Martin J. H., Gordon R. M. and Fitzwater S. E. (1990) Iron in Antarctic waters. *Nature* **345**, 156–
744 158.
745 Massoth, G. J., Baker, E. T., Lupton, J. E., Feely, R. A., Butterfield, D. A., Von Damm, K. L., Roe
746 K. K. and Lebon G. T. (1994) Temporal and spatial variability of hydrothermal manganese and
747 iron at Cleft segment, Juan de Fuca Ridge. *J. Geophys. Res.* **99(B3)**, 4905-4923.
748 Massoth G. J., De Ronde C. E. J., Lupton J. E., Feely R. A., Baker E. T., Lebon G. T. and
749 Maenner S. M. (2003) Chemically rich and diverse submarine hydrothermal plumes of the
750 southern Kermadec volcanic arc (New Zealand). *Geo. Soc. London Special Pub.* **219**, 119-139.
751 Moffett J. W. and German C. R. (2020) Distribution of iron in the Western Indian Ocean and the
752 Eastern tropical South pacific: An inter-basin comparison. *Chem. Geol.* **532**, 119334.
753 Morgan J. L., Wasylenki L. E., Nuester J. and Anbar A. D. (2010) Fe isotope fractionation during
754 equilibration of Fe-organic complexes. *Environ. Sci. Technol.* **44**, 6095-6101.
755 Nasemann P., Gault-Ringold M., Stirling C. H., Koschinsky A. and Sander S. G. (2018) Processes
756 affecting the isotopic composition of dissolved iron in hydrothermal plumes: A case study
757 from the Vanuatu backarc. *Chem. Geol.* **476**, 70-84.
758 Neuholz R., Kleint C., Schnetger B., Koschinsky A., Laan P., Middag R., Sander S., Thal J.,
759 Türke A., Walter M., Zitoun R. and Brumsack H. J. (2020) Submarine hydrothermal discharge
760 and fluxes of dissolved Fe and Mn, and He isotopes at brothers volcano based on radium
761 isotopes. *Minerals* **10**, 969.
762 Nishioka J., Obata H. and Tsumune D. (2013) Evidence of an extensive spread of hydrothermal

763 dissolved iron in the Indian Ocean. *Earth Planet. Sci. Lett.* **361**, 26-33.
764 Rayleigh J. W. S. (1896) Theoretical considerations respecting the separation of gases by diffusion
765 and similar processes. *Phil. Mag., Ser.* **42**, 493-498.
766 Resing J. A. and Mottl M. J. (1992) Determination of manganese in seawater using flow injection
767 analysis with on-line preconcentration and spectrophotometric detection. *Anal. Chem.* **64**,
768 2682-2687.
769 Resing J. A., Lebon G., Baker E. T., Lupton J. E., Embley R. W., Massoth G. J. , Chadwick W. W.
770 and de Ronde C. E. J. (2007) Venting of Acid-Sulfate fluids in a High-Sulfidation setting at
771 NW rota-1 submarine volcano on the mariana arc. *Econ. Geol.* **102**, 1047-1061.
772 Resing J. A., Baker E. T., Lupton J. E., Walker S. L., Butterfield D. A. , Massoth G. J. and
773 Nakamura K. (2009) Chemistry of hydrothermal plumes above submarine volcanoes of the
774 Mariana Arc. *Geochem. Geophys. Geosyst.* **10**, Q02009.
775 Resing J. A., Rubin K. H., Embley R. W., Lupton J. E., Baker E. T., Dziak R. P., Baumberger T.,
776 Lilley M. D., Huber J. A., Shank T. M., Butterfield D. A., Clague D. A., Keller N. S., Merle S.
777 G., Buck N. J., Michael P. J., Soule A., Caress D. W., Walker S. L., Davis R., Cowen J. P.,
778 Reysenbach A. and Thomas H. (2011) Active submarine eruption of boninite in the
779 northeastern Lau Basin. *Nat. Geosci.* **4**, 799-806.
780 Resing J. A., Sedwick P. N., German C. R., Jenkins W. J., Moffett J. W., Sohst B. M. and
781 Tagliabue A. (2015) Basin-scale transport of hydrothermal dissolved metals across the South
782 Pacific Ocean. *Nature* **523**, 200-203.
783 Rouxel O., Toner B. M., Manganini S. J. and German C. R. (2016) Geochemistry and iron isotope
784 systematics of hydrothermal plume fall-out at East Pacific Rise 9°50′N. *Chem. Geol.* **441**,
785 212-234.
786 Rubin, K., and Embley, R. (2012). Identification and Implications of a Submarine Monogenetic
787 Field in the NE Lau Basin. Abstract T51D-2605 presented at 2012 Fall Meeting, AGU, San
788 Francisco, Calif., 3–7 Dec.
789 Rubin K. H. and Shipboard Scientific Party. (2017) 2017 NE Lau Basin Cruise Report for
790 FK171110 on RV Falkor, Honolulu, Seattle, Hi.

791 Sander S. G. and Koschinsky A. (2011) Metal flux from hydrothermal vents increased by organic
792 complexation. *Nat. Geosci.* **4**, 145-150.
793 Sands C. M., Connelly D. P., Statham P. J. and German C. R. (2012) Size fractionation of trace
794 metals in the Edmond hydrothermal plume, Central Indian Ocean. *Earth Planet. Sci. Lett.* **319–**
795 **320**, 15-22.
796 Severmann S., Johnson C. M., Beard B. L., German C. R., Edmonds H. N. and Chiba H. and
797 Green D. R. H. (2004) The effect of plume processes on the Fe isotope composition of
798 hydrothermally derived Fe in the deep ocean as inferred from the Rainbow vent site,
799 Mid-Atlantic Ridge, 36°14′N. *Earth Planet. Sci. Lett.* **225**, 63-76.
800 Tagliabue A., Bowie A. R., Boyd P. W., Buck K. N., Johnson K. S. and Saito M. A. (2017) The
801 integral role of iron in ocean biogeochemistry. *Nature* **543**, 51-59.
802 Toner B. M., Fakra S. C., Manganini S. J., Santelli C. M., Marcus M. A., Moffett J., Rouxel O.,
803 German C. R. and Edwards K. J. (2009) Preservation of iron(II) by carbon-rich matrices in a
804 hydrothermal plume. *Nat. Geosci.* **2**, 197-201.
805 Town R. M. and Filella M. (2000) Dispelling the myths: is the existence of L1 and L2 ligands
806 necessary to explain metal ion speciation in natural waters? *Limnol. Oceanogr.* **45**, 1341–
807 1357.
808 Walker, S. L., Baker, E. T., Lupton, J. E. and Resing, J. A. (2019) Patterns of fine ash dispersal
809 related to volcanic activity at west mata volcano, NE Lau Basin. *Front. Mar. Sci.* **6**, 593.
810 Wang H., Yan Q., Yang Q., Ji F., Wong K. H. and Zhou H. (2019) The size fractionation and
811 speciation of iron in the longqi hydrothermal plumes on the southwest indian ridge. *J. Geophys.*
812 *Res.-Oceans* **124**, 4029-4043.
813 Wang H., Resing J. A., Yan Q., Buck N. J., Michael S. M., Zhou H., Liu M., Walker S. L., Yang
814 Q. and Ji F. (2021a) The characteristics of Fe speciation and Fe-binding ligands in the Mariana
815 backarc hydrothermal plumes. *Geochim. Cosmochim. Acta* **292**, 24-36.
816 Wang W., Lough A., Lohan M. C., Connelly D. P., Cooper M., Milton J. A., Chavagnac V.,
817 Castillo A. and James R. H. (2021b) Behavior of iron isotopes in hydrothermal systems: Beebe
818 and Von Damm vent fields on the Mid-Cayman ultraslow-spreading ridge. *Earth Planet. Sci.*

Lett. **575**, 117200.

Welch S. A., Beard B. L., Johnson C. M. and Braterman P. S. (2003) Kinetic and equilibrium Fe isotope fractionation between aqueous Fe(II) and Fe(III). *Geochim. Cosmochim. Acta* **67**, 4231-4250.

Wu L. L., Beard B. L., Roden E. E. and Johnson C. M. (2011) Stable iron isotope fractionation between aqueous Fe(II) and hydrous ferric oxide. *Environ. Sci. Technol.* **45**, 1847–1852.

Yücel M., Gartman A., Chan C. S. and Luther G. W. (2011) Hydrothermal vents as a kinetically stable source of iron-sulphide-bearing nanoparticles to the ocean. *Nat. Geosci.* **4**, 367-371.

Zellmer K. E. and Taylor B. (2001) A three-plate kinematic model for Lau Basin opening. *Geochem. Geophys. Geosys.* **2**, 1525-2027.

Zhu K., Hopwood M. J., Groenenberg J. E., Engel A., Achterberg E. P. and Gledhill M. (2021) Influence of pH and dissolved organic matter on iron speciation and apparent iron solubility in the Peruvian shelf and slope region. *Environ. Sci. Technol* **55**, 9372-9383.